Ocean Engineering 339 (2025) 122086

Contents lists available at ScienceDirect

Ocean Engineering

journal homepage: www.elsevier.com/locate/oceaneng

Research paper

Reconstructing three-dimensional density from surface data in the North Atlantic Sea through the PIO-Net model

Yuanhong Chen [a,b], Chunxin Yuan [a,b], Xiang Sun [a,b], Zhen Gao [a,b,*]

[a] School of Mathematical Sciences, Ocean University of China, Qingdao, 266100, China
[b] Laboratory of Marine Mathematics, Ocean University of China, Qingdao, 266100, China

ARTICLE INFO

Keywords:
Subsurface density reconstruction
Reduced-order modeling
Physics-informed deep learning
Transfer learning
Argo observations

ABSTRACT

This study evaluates the applicability of the physics-informed operator network (PIO-Net) for reconstructing subsurface density anomalies (SDAs) based on sea surface density. PIO-Net approximates the density field by representing SDAs as a linear combination of reduced-basis, integrating physical constraints by the quasi-geostrophy theory while reducing computational costs. Nevertheless, the original PIO-Net can only tackle the gridded data, contradicting to the fact that the in-situ observations in the vertical column is sparse. To address this limitation, the network's loss function is modified to the mean squared error between the interpolation-based reconstruction and observations. Furthermore, we propose a transfer learning strategy that involves pre-training the model on reanalysis data and subsequently fine-tuning it with sparse Argo observations using the adapted loss function. Validation with independent Argo observations shows that the reconstructed SDAs align well with in situ measurements, with improved accuracy in data-sparse regions. Comparative analyses between the PIO-Net and publicly available grided Argo products exhibit that PIO-Net achieves the accuracy at same order, but with resolution as high as request. In addition, the case study illustrates the PIO-Net outperforms purely data-driven models such as Long Short-Term Memory network and feedforward neural networks. Finally, potential error sources and future extensions are discussed.

1. Introduction

Marine science research is closely related to ocean observations, which enhance the understanding of the structure and dynamic patterns of the ocean, especially given that the ocean covers about 71 % of the Earth's surface and is constantly in motion at various scales under the influence of many factors, including wind, gravity, and human activities, and has a significant impact on global climate change (Trenberth and Fasullo, 2013; Trenberth, 2015; Xie and Yu, 2017). Consequently, there has been a sustained effort to collect continuous, uninterrupted, and well-sampled ocean observations currently characterized by two distinct features. On the one hand, the launch of the Array for Real-time Geostrophic Oceanography (Argo) program has significantly improved the observing capability of key dynamical parameters in the ocean (Dean et al., 2009; Johnson et al., 2022; Roemmich et al., 2009a). However, the costly and time-consuming nature of direct observation of the deep ocean poses significant challenges, and the deployment of Argo floats remains sparse and uneven relative to the vastness of the ocean (Zhou et al., 2023; Roemmich et al., 2009b; Meng and Yan, 2022). On the other hand, advances in remote sensing technology have enabled the acquisition of high-resolution, spatiotemporally continuous ocean observations on a global scale (Torres et al., 2012; Roarty et al., 2019; Xue et al., 2021), leading to significant breakthroughs in marine science (Assassi et al., 2016; Klein et al., 2019), but the satellite observations are limited to ocean surface (Talley et al., 2011).

The existing high-resolution three-dimensional ocean datasets are mostly derived from numerical models (Jean-Michel et al., 2021; Blumberg and Mellor, 1987; Mellor et al., 2002), which have significantly advanced the field of ocean dynamics research. However, these models are susceptible to errors (Fox-Kemper et al., 2019; Stammer, 2005; Tian et al., 2022) due to truncation, parameter uncertainties, and limited observations, as well as being computationally expensive. To maximize the utility of the abundant sea surface observations and to address the pressing research requirements for three-dimensional ocean dynamical processes and climate, many researchers have explored models to predict the ocean interior structure using surface information (Khedouri et al., 1983; Klemas and Yan, 2014), based on the fact that the changes in distribution of multiple sea surface parameters contain a significant amount of information about internal structure and dynamic processes.

---

* Corresponding author.
E-mail addresses: chenyuanhong@stu.ouc.edu.cn (Y. Chen), yuanchunxin@ouc.edu.cn (C. Yuan), sunxiang@ouc.edu.cn (X. Sun), zhengao@ouc.edu.cn (Z. Gao).

https://doi.org/10.1016/j.oceaneng.2025.122086
Received 27 February 2024; Received in revised form 12 June 2025; Accepted 29 June 2025

One sort of approach involves establishing a physical relationship between surface parameters and internal properties, from which internal oceanic information can be derived under certain assumptions (Isern-Fontanet et al., 2006; Lapeyre and Klein, 2006; Klein et al., 2009; Wang et al., 2013). In particular, the theoretical method based on quasi-geostrophy (QG) (Held et al., 1995) has been widely used as a simplified framework for depicting fundamental flow in ocean. Effective surface QG (eSQG) (Lapeyre and Klein, 2006) and interior plus surface QG (isQG) (Wang et al., 2013) are two typical methods, where the former assumed surface density and interior potential vorticity (PV) are well-correlated to overcome the challenge of missing internal PV, verified with model simulation data (Isern-Fontanet et al., 2008; Qiu et al., 2016). To overcome the limitation of eSQG, which becomes less applicable when the correlation between sea surface height (SSH) and sea surface density (SSD) is weak, isQG decomposes the subsurface state field into two distinct components, which are solved independently using SSH and SSD. isQG was examined by evaluation with high-resolution ocean model data (Liu et al., 2019) and reanalysis datasets (Chen et al., 2020; Liu et al., 2014, 2017), showed superior performance and yielded promising results. Nevertheless, models based on simplified dynamics are constrained to specific conditions and inevitably require repeated model solving.

Compared with the aforementioned methods, data-driven approaches offer a more straightforward construction process, requiring only training, testing, and utilizing the trained model for evaluation (Doshi-Velez and Kim, 2017; Guo et al., 2016). Given appropriate training, estimation of underwater information can be performed quickly by feeding available sea surface data into the model. Data-driven models, which can be based on either traditional statistical methods or machine learning methods, establish relationships between sea surface parameters and target parameters. In contrast to traditional statistical methods (Fiedler, 1988; Fischer et al., 1997; Carnes et al., 1994; Guinehut et al., 2012; Gallaudet and Simpson, 1994; Maes et al., 2000; Buongiorno Nardelli and Santoleri, 2005; Buongiorno Nardelli et al., 2012), machine learning techniques derive relationships directly from the data and demonstrate superior performance. Examples include artificial neural network (Ali et al., 2004; Bao et al., 2019; Su et al., 2020), self-organizing maps (Wu et al., 2012; Chen et al., 2018), support vector machine (Su et al., 2015, 2018), clustering neural network (Lu et al., 2019), and random forest (Su et al., 2018). Recently, deep learning's success in capturing complex information through intricate network architectures and algorithms presents a new opportunity for marine scientific research. In particular, long short-term memory network (Buongiorno Nardelli, 2020b; Su et al., 2021b; Contractor and Roughan, 2021) and convolutional neural networks (Meng et al., 2021; Su et al., 2021a; Meng et al., 2022) have proven to be powerful in three-dimensional ocean reconstruction, surpassing the performance of conventional machine learning methods. However, this type of approach has limitations as there is no explicit physical explanation and the underlying physical relationships of the model remain ambiguous (Dong et al., 2022; Wang et al., 2021).

To combine the advantages of the two class methods, Chen et al. (2024) proposed a physics-informed deep operator learning network model, PIO-Net, for estimating subsurface density anomaly (SDA) profiles. The PIO-Net model is established on the framework of the QG equation and incorporates unknown functions learned from the data to construct a dynamic equation that describes both the surface and interior. To leverage the knowledge in the dynamic equation and in the data, PIO-Net represents the SDA profile as a linear combination of a set of reduced-basis, trained with the constructed equation as constraints and combined with collected data. The inputs to this model are SSD anomaly coefficients and depth, and output is SDA coefficients. Simulations from the numerical model are used to validate the PIO-Net, showcasing excellent agreement between the density field estimated by PIO-Net and the simulations while demonstrating the strong generalization capability of PIO-Net. However, PIO-Net is an exploratory attempt to integrate physical dynamics with deep learning, several challenges remain to be addressed. First, the current evaluation of PIO-Net is based solely on the grided data of ocean model simulations. Compared to observational data, numerical simulations eliminate many sources of uncertainty, which may lead to overestimated model performance. Therefore, it is necessary to validate the proposed framework using more realistic data to ensure its flexibility. Second, PIO-Net is more suitable for gridded data, whereas observations are often sparse and irregularly distributed. With the rapid advancements in observation and computer technology, the potential of PIO-Net should be explored further. This study is primarily aimed at addressing these two challenges.

In this work, the applicability of PIO-Net in the North Atlantic Sea is first explored using Hybrid Coordinate Ocean Model (HYCOM)/Navy Coupled Ocean Data Assimilation (NCODA) reanalysis data (Chassignet et al., 2007), which are considered to be more realistic compared to pure numerical models. However, applying PIO-Net directly to observational data presents several challenges due to the sparse and irregular distribution of Argo floats. To address these issues, we modify the loss function to incorporate observational constraints. Furthermore, to enhance the model performance, we develop a new strategy for constructing high-resolution SDAs in the real ocean. This framework begins by constructing mappings from observed locations to basis functions using bicubic spline interpolation, enabling the reconstruction of SDAs at arbitrary positions. The training of PIO-Net is divided into two stages to integrate physical relationships derived from reanalysis data and enhance consistency with observational data. In the first stage, PIO-Net is pre-trained using reanalysis data. In the second stage, the pre-trained model is fine-tuned with sparse observations, where the loss function is modified to the mean squared error between the observed and reconstructed SDAs. To evaluate the reliability of the reconstructed SDAs, we conduct comparisons with independent Argo observations and gridded Argo products. These SDAs are estimated as a linear combination of interpolated reduced bases, using coefficients predicted from satellite-derived SSD inputs. To further assess the performance of the proposed method, comparisons are also made with baseline data-driven models in terms of both accuracy and inference efficiency. In addition, the effects of training data size and the role of pre-training on reconstruction accuracy are systematically examined.

The paper is organized as follows. Section 2 introduces the methods which are used to derive the SDA structure from reanalysis data and observations. Section 3 provides the information about the data and experimental setup. Results of the reconstruction and evaluation are fully discussed in Section 4. Finally, a brief concluding is given in Section 5.

2. Methods

2.1. The physics-informed operator learning network of reduced-order model

The method applies PIO-Net to reconstruct three-dimensional ocean density assuming that the flow function $\boldsymbol{\Psi}_h(z,\mathbf{X})$ on a fixed horizontal grids $\mathbf{X} = [x_1\ x_2\ \dots\ x_{N_h}]$ can be represented as a linear combination of reduced-basis, in the following form

$$\boldsymbol{\Psi}_h(z,\mathbf{X}) \approx \sum_{i=1}^{n} \alpha_i(z)\psi_i(\mathbf{X}) = \mathbf{V}\boldsymbol{\alpha}(z), \tag{1}$$

where $\psi_i(\mathbf{X})(i = 1, 2 \dots, n)$ denote the reduced-basis, $\mathbf{V} = [\psi_1(\mathbf{X})\ \ \psi_2(\mathbf{X})\ \ \dots\ \ \psi_n(\mathbf{X})]$, $\boldsymbol{\alpha}(z) = \left[\alpha_1(z)\ \alpha_2(z)\ \dots\ \alpha_n(z)\right]^{\mathrm{T}}$ is the coefficient vector, and the superscript T represents vector transpose. The density anomaly can be estimated as

$$\boldsymbol{\rho}^a = -\frac{\rho_0 f_0}{g}\frac{d\boldsymbol{\Psi}_h}{dz} \approx -\frac{\rho_0 f_0}{g}\frac{\mathbf{V}d\boldsymbol{\alpha}}{dz} = -f\mathbf{V}\frac{d\boldsymbol{\gamma}}{dh},$$

where f_0 is the mean Coriolis parameter, ρ_0 denotes the volume mean density, $f = f_0 \times 10^5$, $\boldsymbol{\gamma} = \rho_0\boldsymbol{\alpha}(500g)^{-1} \times 10^{-5}$, and $h = z/500$.

In order to quickly estimate γ by leveraging the power of deep learning, a combined network PIO-Net with output G_{PI} is proposed to approximate γ, and its inputs are $\boldsymbol{u} = f^{-1}\mathbf{V}^{\mathrm{T}}\boldsymbol{\rho}_0^a$ related to SSD anomaly $\boldsymbol{\rho}_0^a$ and $\boldsymbol{y} = h$ related to depth. The loss function $\mathcal{L}(\theta)$ of the PIO-Net is made up two parts

$$\mathcal{L}(\theta) = c_1\mathcal{L}_{\mathrm{operator}}(\theta) + c_2\mathcal{L}_{\mathrm{physics}}(\theta), \tag{2}$$

where $\mathcal{L}_{\mathrm{operator}}(\theta)$ is the data constraint, consisting of the mean square error between the estimation of PIO-Net and target coefficient, $\mathcal{L}_{\mathrm{physics}}(\theta)$ is the physical constraint, consisting of the residuals of a set of sampling points on the governing equation Eq. (A.2), c_1 and c_2 are the weight coefficients. A detailed description of this method is given in Appendix A.

The efficacy of PIO-Net has been verified in several subdomains with the simulations, which represent an idealized oceanic data far from an real observing system scenario. And it is necessary to evaluate the proposed PIO-Net in different regions using more realistic ocean data. The reanalysis data utilizes ocean observations to correct the numerical solutions, rendering a more accurate ocean state estimation compared to pure numerical models. And the spatiotemporal coverage of the reanalysis data is extensive, providing a more comprehensive and long-term record of ocean conditions compared to observational data. As a result, this study first evaluates the reliability of the PIO-Net trained with reanalysis data in the parts of the North Atlantic.

2.2. PIO-Net for observations

PIO-Net is suitable for gridded data, such data inevitably carries errors compared to in-situ measurements. Furthermore, due to the sparse and non-gridded distribution of Argo floats, the direct application of PIO-Net to Argo observation data presents challenges. Therefore, in order for PIO-Net to be applicable to Argo observations and provide more reliable estimates in the real ocean, the loss function of PIO-Net is reorganized in this section to incorporate observation constraints in the training process and improve the consistency of PIO-Net's output with observations. It can be seen from Section 2.1, the density anomaly at depth z can be approximated as follows

$$\boldsymbol{\rho}^a(z,\mathbf{X}) \approx v^1\boldsymbol{\psi}_1(\mathbf{X}) + v^2\boldsymbol{\psi}^2(\mathbf{X}) + \ldots + v^n\boldsymbol{\psi}_n(\mathbf{X}) = \mathbf{V}\boldsymbol{\nu}, \tag{3}$$

where $\boldsymbol{\nu} = -f\frac{d\gamma}{dh} = \left[v^1\ v^2\ \ldots\ v^n\right]^{\mathrm{T}}$. Furthermore, the density anomaly $\rho^a(z,x^*)$ at any given position (z,x^*) can be represented by the state vector $\boldsymbol{\rho}^a(z,\mathbf{X})$

$$\rho^a\left(z,x^*\right) = \mathcal{H}(\boldsymbol{\rho}^a(z,\mathbf{X})), \tag{4}$$

where $\mathcal{H}$ is the observation operator, typically obtained through interpolation. In this paper, bicubic spline interpolation is adopted, to substitute Eq. (4) into Eq. (3), we have

$$\begin{aligned}\rho^a\left(z,x^*\right) &= \mathcal{H}(\boldsymbol{\rho}^a(z,\mathbf{X}))\\ &\approx \mathcal{H}\left(v^1\boldsymbol{\psi}_1(\mathbf{X}) + v^2\boldsymbol{\psi}_2(\mathbf{X}) + \ldots + v^n\boldsymbol{\psi}_n(\mathbf{X})\right)\\ &= v^1\mathcal{H}\boldsymbol{\psi}_1(\mathbf{X}) + v^2\mathcal{H}\boldsymbol{\psi}_2(\mathbf{X}) + \ldots + v^n\mathcal{H}\boldsymbol{\psi}_n(\mathbf{X})\\ &:= v^1\psi_1(x^*) + v^2\psi_2(x^*) + \ldots + v^n\psi_n(x^*).\end{aligned}$$

Therefore, to reconstruct density anomaly at any given location x^* requires establishing the mappings between x and $\psi_i(x)$ $(i = 1,2,\ldots,n)$.

Suppose there is a set of observations at K locations $\{x_{obs_1}, x_{obs_2}, \ldots, x_{obs_K}\}$, and let ρ_{jk}^a represent the density anomaly at (z_j, x_{obs_k}). To reduce observation error $\|\rho^a - \mathcal{H}(\boldsymbol{\rho}^a)\|$ in the density anomaly reconstructed by PIO-Net, the loss function $\mathcal{L}(\theta)$ is adjusted to

$$\mathcal{L}(\theta) = c_1\mathcal{L}_{\mathrm{data}}(\theta) + c_2\mathcal{L}_{\mathrm{physics}}(\theta), \tag{5}$$

where

$$\mathcal{L}_{\mathrm{data}}(\theta) = \frac{1}{Km}\sum_{k=1}^{K}\sum_{j=1}^{m}\left|\sum_{i=1}^{n} v_{\mathrm{PI}}^i\psi_i(x_{obs_k}) - \rho_{jk}^a\right|^2,$$

v_{PI}^i is an estimate of v^i by PIO-Net and m is the number of vertical levels. Therefore, before training the PIO-Net, a two-dimensional interpolation is only required to compute the value of the basis function at the observation points, and there is no need to repeatedly apply the observation operator $\mathcal{H}$ to the reconstruct density anomaly vector in the PIO-Net training process, as the basis function is independent of time and depth, which will greatly reduce the training time of the network.

The distribution of Argo floats in time and space is sparse and uneven, and it is challenging to train PIO-Net in areas where observations are scarce. To alleviate this problem, we divided the training of PIO-Net into two stages, the first stage involves pre-training the PIO-Net with reanalysis data to learn the rules generally applicable in the ocean. And in the second stage, the pre-trained PIO-Net is fine-tuned with the observational dataset. The specific flowchart for SDAs estimation via PIO-Net with observations is shown in Fig. 1, firstly, the HYCOM data is utilized to compute the reduced-basis and to pre-train the PIO-Net, with

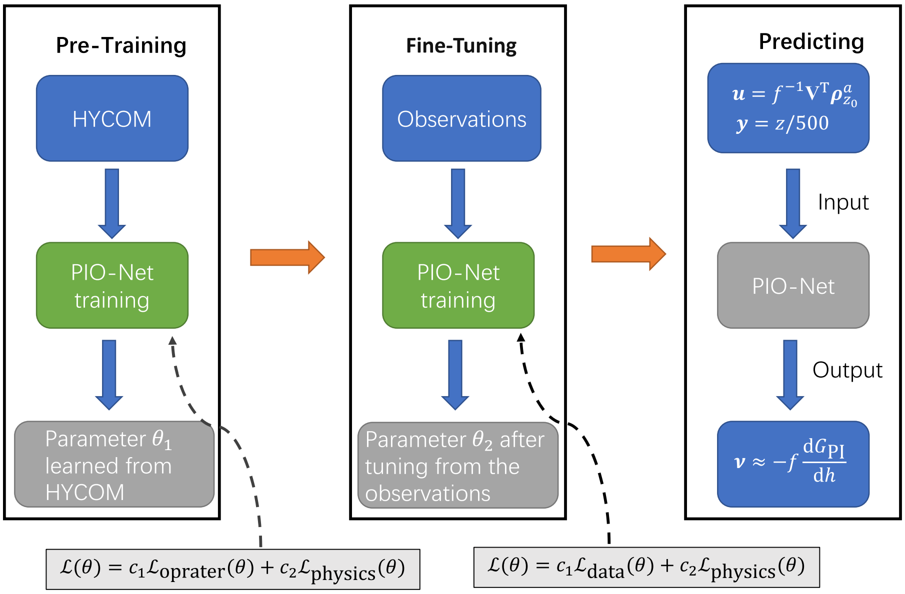

Fig. 1. Flowchart for SDAs estimation via PIO-Net using observations.

the hyperparameter in the trained PIO-Net denoted as θ_1. Then, bicubic spline interpolation is performed to establish the mappings between the coordinates x and the basis functions $\psi_i(x)(i = 1, 2\ldots, n)$, which allows calculating the value of the basis function at any observed position. Subsequently, PIO-Net is re-trained to fine-tune the parameter θ_1 and obtain the parameter θ_2 using observations. After two stages of training, knowledge can be transferred from the reanalysis data, enhancing model performance despite limited observational data. Finally, the density anomaly profile is reconstructed by Eq. (3) with $\boldsymbol{\nu} \approx -f\frac{dG_{\mathrm{PI}}}{dh}$ applying the well-trained PIO-Net.

3. Data and experimental setup

3.1. Reanalysis data sets

The HYCOM/NCODA Global reanalysis data set is first applied to evaluate the PIO-Net model, which was provided by the ocean forecast model HYCOM using the NCODA system by absorbing global observations such as multi-source satellite observations, buoy observations (Cummings, 2005; Cummings and Smedstad, 2013), and in-situ measurements. HYCOM is a global ocean circulation model, which characterized by a vertical mixed coordinate model of isopycnal coordinate, Z coordinate and σ coordinate. The published reanalysis product has a spatial resolution of $1/12°$ and a non-uniform vertical levels (from 0 m to 5500 m). In the context of this study, we focus on a central sub-region within the North Atlantic Ocean that is far away from continental boundaries, shown in Fig. 2 marked by red boxes. And the temperature and salinity variables from the HYCOM for the year 2012 are selected and interpolated onto a horizontal grid with a spatial resolution of 4 km by bicubic spline in this study.

3.2. Observational data sets

To further investigate the applicability of PIO-Net in different regions model using observational data, we chose several regions (marked by blue and red boxes in Fig. 2) in the central North Atlantic with little latitudinal difference, given the similarity of dynamical processes in these regions and the distribution of Argo floats sufficient to test the proposed model. The satellite observations and Argo floats in 2012 for this regions are collected. The input requisites for the PIO-Net included SSD and depth data. The former used in this work is a level 4 (L4) product developed as part of the European Space Agency World Ocean Circulation project (ESA-WOC) (Buongiorno Nardelli, 2020a), which combines high-resolution satellite SST measurements with in-situ measurements of salinity and density, and the RMSE ranges of $0.09 - 0.32\ \mathrm{kg/m^3}$ for SSD.

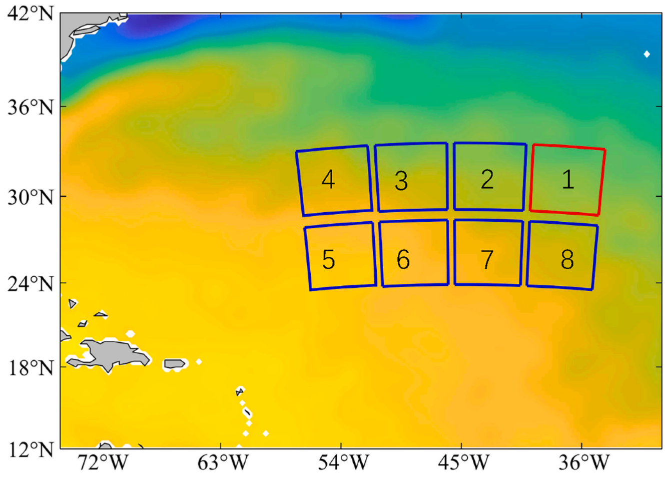

Fig. 2. Fields of SST from WOA18 in June.

The Argo dataset used in this study is from the global ocean Argo temperature and salinity profile scatter dataset (Liu et al., 2021), provided by the Argo Real-time Data Center in China. To improve data quality, the post-quality control procedure developed by CARDC was applied to rigorously screen all profile data. Specifically, we retained only the profiles with a quality control flag of 1—which corresponds to “Good data” according to the Argo real-time and delayed-mode quality control manuals—and with thermohaline measurements extending to at least 1200 m. Each vertical profile is then interpolated to standard depth levels using cubic spline interpolation.

3.3. Gridded argo products

Monthly global gridded datasets, namely EN4 from the Met-Office (Good et al., 2013) and GDCSM_Argo (Zhang et al., 2022) from Shanghai Ocean University, are used to compare the reconstructed density fields. The EN4 dataset spans from 1900 to the present and is based on subsurface ocean temperature and salinity profiles from the WOD09, GTSPP, Argo, and ASBO collections. It is characterized by a regular 1° horizontal grid and contains 42 vertical levels. GDCSM_Argo is constructed using gradient-dependent optimal interpolation and a pycnocline-based model, covering the period January 2004 to December 2020, with a spatial resolution of $1° \times 1°$ and a total of 58 vertical levels segmented at depths below 2000 m.

3.4. Data processing

The temperature and salinity are utilized to calculate density by the state equation provided by Fofonoff and Millard (1983). The density anomaly field is filtered from the monthly climatological density field, which is also calculated by the temperature and salinity data from monthly World Ocean Atlas 2018 (WOA18) through the state equation (Fofonoff and Millard, 1983). And to ensure that the vertical resolution of the computed density climatology consistent with the vertical resolution of HYCOM reanalysis data, linear interpolation is carried out. Then the interpolated climatology remapped onto a grid that aligns with the obtained density field using the bicubic spline interpolation. And the global gridded Argo products are interpolated to the spatio-temporal position of the in-situ observations for comparison.

3.5. Experimental setup

The performance of PIO-Net is first evaluated in Section 4.1 with HYCOM reanalysis data, where the number of neurons in the hidden layer of PIO-Net is 100 and weight coefficients $c_1 = 5$ and $c_2 = 1$, while the remaining settings are configured according to Section 4.1 of Chen et al. (2024). A detailed description of the training process and density reconstruction utilizing reanalysis data can be provided by Chen et al. (2024). The process of training PIO-Net with observations in Section 4.2 is mainly discussed in this section. In the pre-training stage, the settings of PIO-Net and the training data are the same as those in Section 4.1. In the subsequent fine-tuning stage, the loss function Eq. (5) is applied with weight coefficients $c_1 = 30$ and $c_2 = 1$ to emphasize the significance of observational constraints. And the vertical residuals is half uniformly selected from the residuals in the pre-training stage. In addition, it should be noted that to test the trained PIO-Net with observetions, the established mappings $\psi_i(x)(i = 1, 2\ldots, n)$ are used to generate the function value at the test position. The coefficient $\boldsymbol{\nu}_{\mathrm{PI}}$, approximated by the PIO-Net, is then used to compute the density anomaly at the test position, allowing for comparison with the observitions.

4. Results

4.1. Evaluation of reconstruction based on HYCOM data

To evaluate the influence of the number of reduced-basis on accuracy of reconstruction, the PIO-Net models with varying reduced-basis are

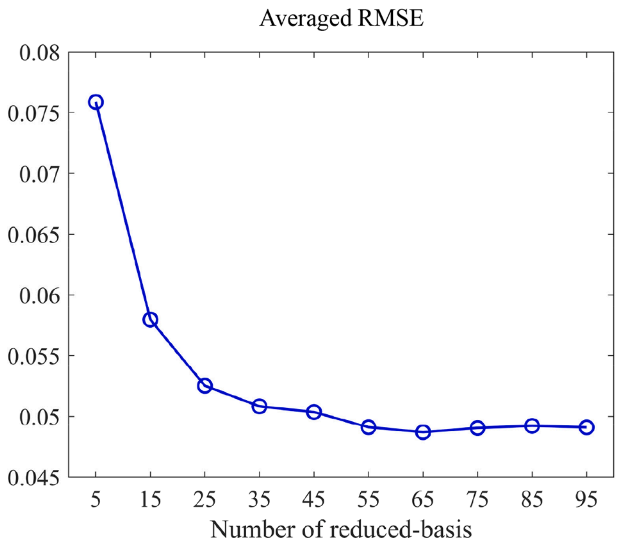

Fig. 3. Prediction errors for the PIO-Net with different number of reduced-basis.

constructed. The accuracy of the reconstruction is reflected by the root mean square error (RMSE) and the averaged RMSE, where the RMSE is defined as

$$\text{RMSE} = \sqrt{\frac{1}{N_h}\left\|\rho_i^a - \hat{\rho}_i^a\right\|_2^2},$$

with N_h is the number of horizontal grid points in the reconstructed region, which is depth and time dependent and represents the difference between the predicted density anomaly $\hat{\rho}^a$ and the observed density anomaly ρ^a at different times and depths. The time-averaged RMSE is depth dependent and is computed as the mean of the RMSEs across all test instances and represents the vertical distribution of the difference between predicted and real density anomalies. The time-depth averaged RMSE is calculated as the mean of the RMSEs across all test instances and depths.

Fig. 3 shows the time-depth averaged RMSEs estimated by PIO-Net with different number of reduced-basis. As can be seen from the Fig. 3, increasing the reduced-basis at the start results in a decrease in the prediction error, suggesting that increasing the number of reduced-basis functions improves the prediction accuracy within a certain range. However, the improvement in accuracy is limited, increasing the number of reduced-basis does not always better. An overly extensive reduced-basis may produces negative impacts on the model's performance, as an excessive number of reduced-basis capture subtle variations in the training data instead of focusing on the primary features, making it difficult to generalize to new data. Another possible reason is that the number of training data currently collected is insufficient to produce accurate high-frequency signatures, and the reduced-basis generated from this data is not sufficient to represent all state vectors. The PIO-Net model with 65 reduced-basis achieved the best reconstruction, and corresponding time-averaged RMSE for the estimated profiles and HYCOM is exhibited on the left side of Fig. 4, with values less than 0.08. Notably, there are three prominent peaks observed at depths of 50 m, 150 m and 500 m, respectively, which potentially correlate with the influence of the halocline, mixed layer, and thermocline changes.

Furthermore, the right panel of Fig. 4 shows the time-averaged root mean square (RMS) of the density anomaly for HYCOM and the PIO-Net model, displaying significant agreement and consistent changes, particularly in the upper layers where the density variations are strong. The PIO-Net model gives consistently reliable reconstructions, highlighting its effectiveness in estimating the distribution of SDAs based on surface information. To further evaluate the reconstruction performance, the density anomaly distributions at 150 m depth from both the PIO-Net model and HYCOM for three different times are presented in Fig. 5. The density anomaly distributions derived from the PIO-Net are extremely promising, closely matching those derived from HYCOM. The slight differences between the two are mainly located in the northeast of the test

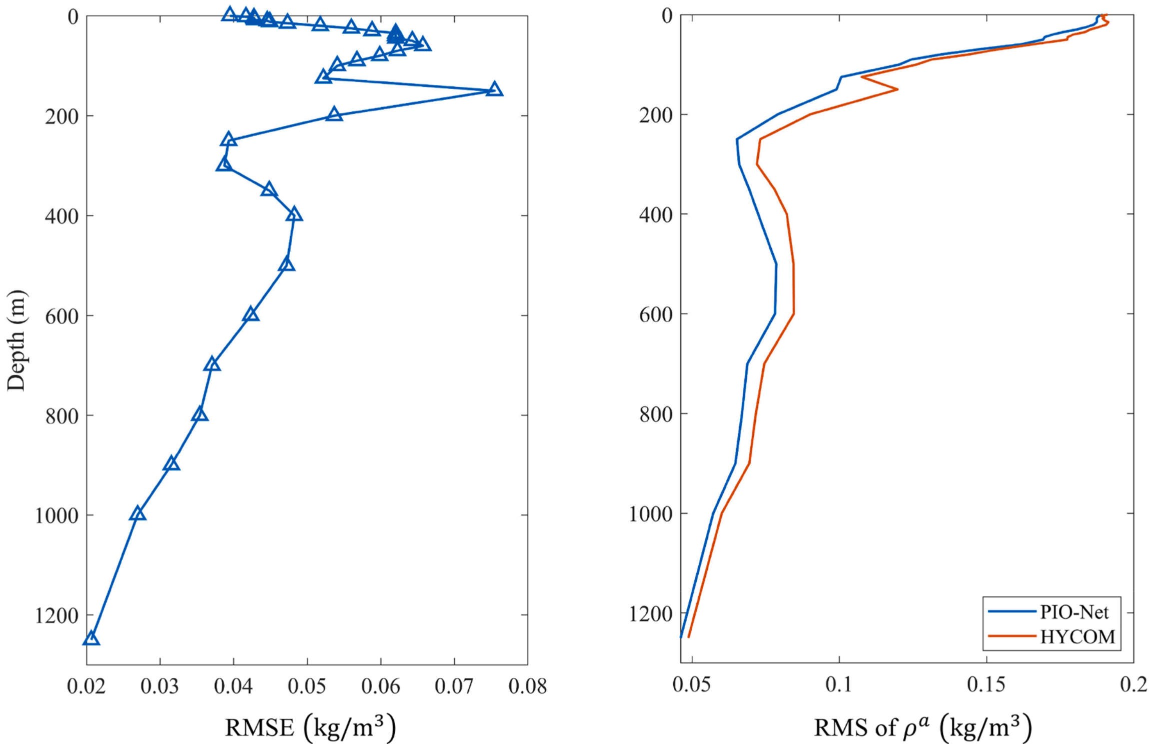

Fig. 4. Left: Time-averaged RMSE of density anomalies between the original reanalysis data and reconstructed profiles, and Right: time-averaged RMS of the density anomaly derived from PIO-Net (blue solid line) and HYCOM (orange solid line).

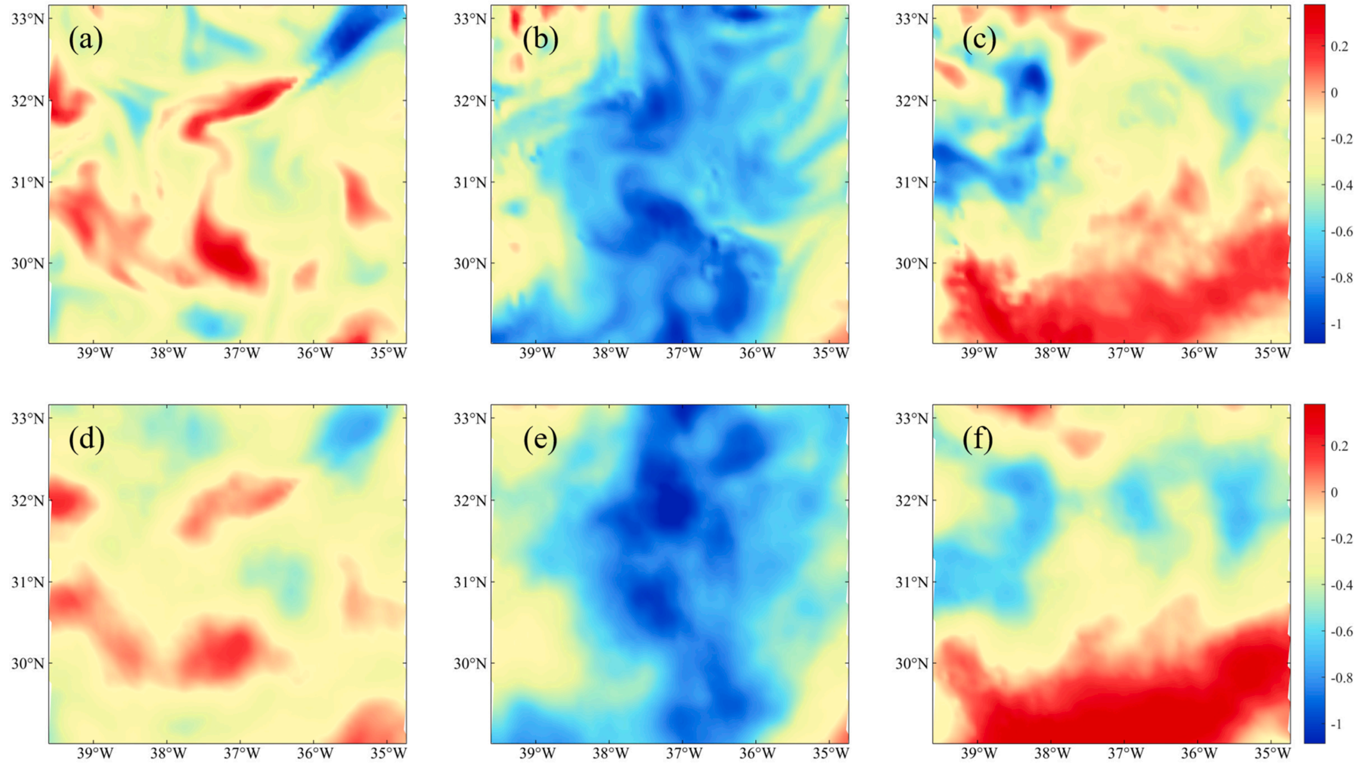

Fig. 5. Density anomalies from HYCOM (top) and from the PIO-Net (bottom) at March 15th (a, d), June 18th (b, e) and September 15th (c, f).

region on June 16th. The reason could be that the numerous eddies present along the Gulf Stream pathway, resulting in intricate oceanic dynamical processes, and due to the simplification of reduced-order modeling, the reduced-basis is lacking in describing small structures. In general, the PIO-Net model accurately captures the characteristics of density anomaly distributions, including both positive and negative patterns and finer-scale structures, particularly the density structures south of 30° N on September 15th, which indicates that the performance of the reconstruction with PIO-Net is time-dependent and may not be as effective in summer as in other seasons, possibly because the summer mixed layer is shallower and the thermocline is stronger due to surface warming.

4.1.1. *Sensitivity analysis and methods comparison*

In this section, we investigate the impact of network structure by varying the number of neurons in the hidden layers, and the models are computed using a laptop with 4 Intel(R) Core(TM) Ultra 5-125H @1.20 GHz and 8G Memory. Table 1 presents the training time, testing time, and prediction accuracy for different neuron configurations. As the number of neurons increases, both the training and testing times rise significantly. Specifically, the training time increases from approximately 1440.79 s to 8282.66 s as the number of neurons grows from 50 to 250, while the testing time rises from 1.29 s to 3.99 s. This indicates that models with more complex architectures require greater computational resources. Notably, while increasing the number of neurons leads to a substantial rise in training time, the testing time remains relatively low in comparison, indicating that once trained, the model can make fast predictions even with a complex architecture. At the same time, the prediction error gradually decreases from 0.0578 to 0.0433, suggesting that increasing the number of neurons can improve model accuracy. However, the marginal improvement in accuracy diminishes as the network size increases, therefore, in practical applications, an appropriate network size can be selected to balance the prediction accuracy and computational efficiency.

Table 1
The mean RMSE and the CPU time for the different number of neurons in hidden layers.

The number of neurons	50	100	150	200	250
Training time (s)	1440.79	2307.21	3372.18	5919.93	8282.66
Testing time (s)	1.29	1.75	2.54	3.02	3.99
Prediction errors	0.0578	0.0491	0.0465	0.0444	0.0433

To further evaluate the performance of PIO-Net, we compare the results obtained by the PIO-Net with 250 neurons (using 55 basis functions) against two commonly used data-driven models: U-Net (Yu et al., 2025; Ronneberger et al., 2015) and Convolutional Long Short-Term Memory (ConvLSTM) (Xu et al., 2025; Shi et al., 2015). Both models take the sea surface density anomaly as input and aim to predict subsurface ocean density anomalies. The U-Net adopts an encoder—decoder structure with skip connections. The encoder consists of four stages of convolutional layers with batch normalization and ReLU activations, each followed by max pooling to reduce spatial resolution. The number of channels increases from 32 to 512 across the encoder, with kernel size 3×3. The decoder upsamples the feature maps using transposed convolutions and merges them with corresponding encoder outputs via skip connections. A two-layer ConvLSTM is employed with hidden dimensions $[64, 34]$, and 3×3 kernels. The batch size is set to 8, with 1000 epochs for U-Net and ConvLSTM model.

It is worth noting that we do not perform an exhaustive search for the optimal architectures or hyperparameters for each model, instead, we adopt standard implementations commonly used in practice. Therefore, the reported results do not necessarily represent the best achievable performance for all the models. As shown in Table 2, PIO-Net demonstrates significantly lower training and testing times compared to both baselines. Specifically, PIO-Net achieves a 3.65-fold reduction in training time and a 32.27-fold speed-up in inference compared to U-Net, while maintaining comparable accuracy, as illustrated in Fig. 6. Although ConvLSTM is relatively faster than U-Net, its prediction

Table 2
Training and inference times of different models, and the speed-up of PIO-Net relative to each baseline.

Method	Training time (s)	Speed-up of PIO-Net	Testing time (s)	Speed-up of PIO-Net
U-Net	30209.81	3.65	128.75	32.27
ConvLSTM	12734.18	1.54	10.95	2.74

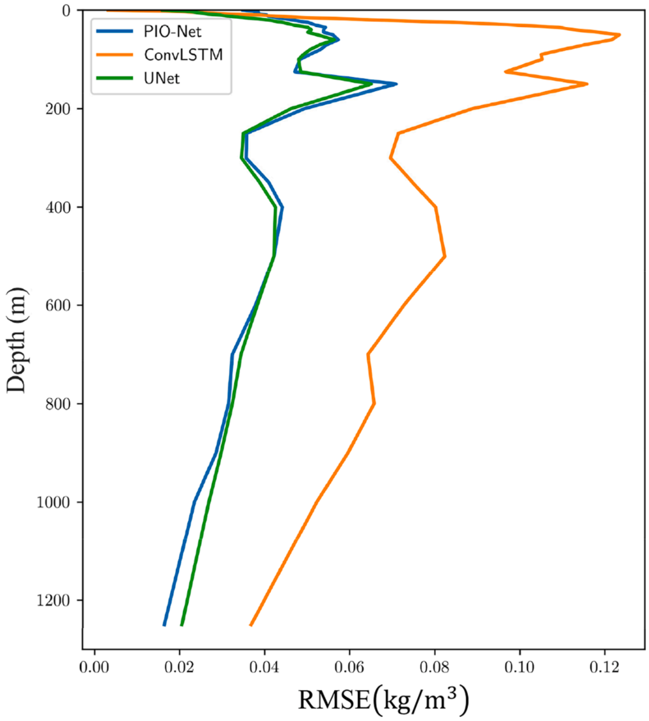

Fig. 6. Prediction errors for different methods.

accuracy is considerably lower. These results confirm the effectiveness of the proposed approach in reconstructing subsurface ocean density anomalies.

4.2. Evaluation of reconstruction based on observations

In this section, the performance of the improved PIO-Net model with observations is verified through various experiments using data collected from different regions. For all experiments, the data gathered is divided into two distinct parts, with eighty percent used to train the PIO-Net model and the remaining twenty percent reserved as a test set to examine the reconstruction performance.

To evaluate the regional dependency of PIO-Net, as well as the impact of training data size on the model, three experiments with different training data are carry out. The first experiment, exp1, is based on data from region 1, while the second experiment, exp2, utilizes data from regions 1 to 4, and the third experiment, exp3, employs data from regions 1 to 8. The number of observations in both the train and test sets is provided in Table 3. In addition, subdomains at similar latitudes share a common set of reduced-basis, specifically, the reduced-basis for regions 1–4 is derived from HYCOM data in region 1, whereas the reduced-basis for regions 5–8 is calculated using HYCOM data from region 8. The ability of the reduced-basis to represent the density anomaly field can be seen in Fig. 7, which shows the distribution of SSD anomalies represented by the reduced-basis in exp3 and provided by ESA-WOC for two randomly selected regions and times in the test dataset. A striking similarity between the two is evident, implying that the reduced-basis can effectively represent the satellite-derived SDA field by applying appropriate coefficients.

Table 3
The number of observations in both the training and test sets.

	Training data size	Testing data size
exp1	63	16
exp2	174	44
exp3	705	176

Fig. 8 displays the time-depth averaged RMSEs estimated by PIO-Net for three distinct data configurations against the number of reduced-basis. It is important to note that when the number of reduced-basis is greater than 5, there is no significant difference between prediction accuracy and the number of reduced-basis. The reason could be that the use of HYCOM data to construct the reduced-basis is limited to representing only the low-frequency features of the observed data. Even with an increase in the number of reduced-basis, an accurate representation of the high-frequency features remains elusive due to the differences between HYCOM and the observed data. Therefore, augmenting the number of reduced-basis within a specified range enhances the model's representation ability for HYCOM, but it may not be more appropriate for observations.

In addition, the effect of the pre-training strategy on the accuracy of PIO-Net is also under investigation. Specifically, we train the PIO-Net models solely on observations without adjusting according to the pre-trained model (i.e. there is no pre-training phase). Similar estimation errors are also depicted in Fig. 8, comparison of prediction errors from these three experiments shows that the performance of the PIO-Net model improves with the enrichment of the training data in the absence of a pre-training phase. However, utilizing knowledge derived from HYCOM data has the potential to enhance the predictive accuracy of the PIO-Net model when the data is insufficient. This enhancement is especially evident in exp1, on the one hand, because there is little training data in exp1, and insufficient data leads to limited knowledge and overfitting of the model. Learning certain general features from HYCOM data can mitigate these challenges to some extent, allowing the PIO-Net model to offer more reliable predictions when observational data is limited. Another reason for the improved model performance in exp1 is that the HYCOM data used for pre-training is also from region 1, making the dynamic processes contained in the pre-training and fine-tuning data more similar. However, exp3 shows that when the amount of data is large enough, the implementation of pre-training does not significantly improve the model's accuracy. In summary, the pre-training strategy is most effective when the training data is inadequate, and the information used in the pre-training and fine-tuning stages is similar.

Based on the prediction errors displayed in Fig. 8, the three experiments with the smallest error are selected: exp1 with 75 reduced-basis, exp2 with 75 reduced-basis, and exp3 with 85 reduced-basis without pre-training. And Fig. 9 presents the vertical distribution of the mean of densities from the selected different models. In all three experiments, the PIO-Net models have shown excellent reconstruction results, closely matching the observed density. In particular, exp1 shows a distribution in line with the observed density trends despite limited training data (with only 65 observations used to train the model), although the capture of densities above 100 m is slightly overestimated. In exp2 and exp3, the PIO-Net models accurately capture the density change and are in general agreement with the observed data. These findings demonstrate the potential of the PIO-Net model to provide accurate reconstructions even when observations are limited.

Furthermore, Fig. 10 shows the horizontal distributions of observed and PIO-Net estimated density anomalies in exp3 at 50 m depth, where the error is noticeable, 200 m depth, where temperature fluctuation is significant, and 700 m depth to assess the reliability of the PIO-Net method. At all depths, the two models show a general similarity in

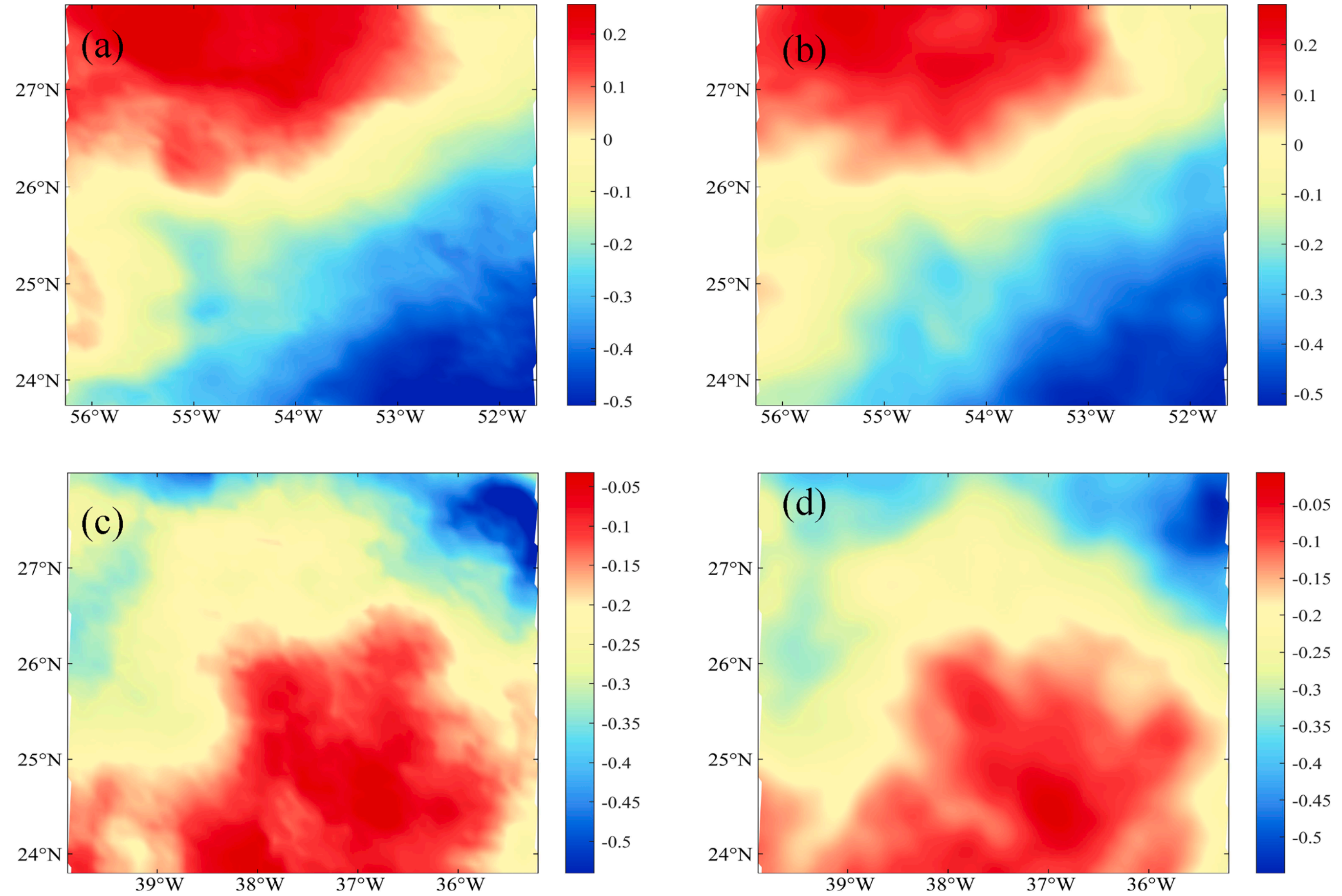

Fig. 7. SSD anomalies from ESA-WOC (a, c) and approximated by reduced-basis (b, d).

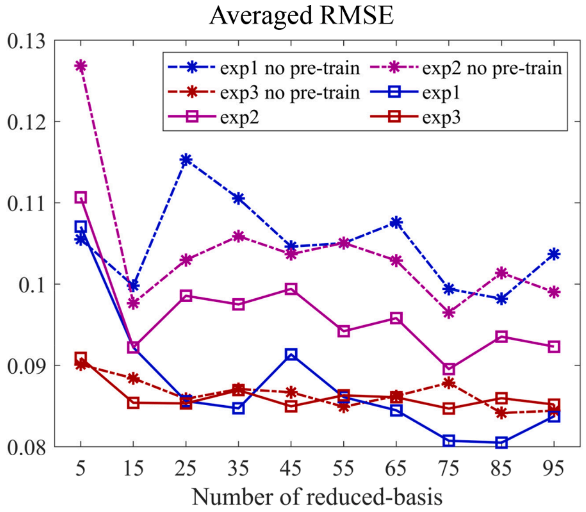

Fig. 8. Prediction errors for observations with different number of reduced-basis.

distribution. Small errors are also shown at depths of 50 m and 200 m in regions with fewer Argo observation points. And obviously, the error of PIO-Net is smaller at 700 m depth, possibly due to the deeper ocean undergoes fewer changes, and physical limitations aid in deep estimation. This demonstrates the practicality of utilizing the PIO-Net approach to estimate subsurface from the sea surface, reflecting the success of introducing physical constraints.

4.2.1. *Comparison with gridded Argo products*

To further verify the reliability of the reconstructed density field, we compare the 2012 GDCSM_Argo, EN4, and the reconstructed density field by interpolating them to the spatio-temporal positions consistent with the Argo floats, and calculate the RMSE between the different products and Argo, which is shown in Fig. 11. The solid orange line in Fig. 11 with legend WOA represents the original Argo observation subtract the monthly WOA18 error. It is obvious that PIO-Net significantly reduces the difference of WOA18 compared to the observation, particularly above 200 m. The RMSE of PIO-Net, GDCSM_Argo, and EN4 products shows a similar trend, with the maximum RMSE at 60 m being 0.10, 0.15 and 0.17 for the training set and 0.16, 0.15 and 0.16 for the testing set. In the training set, PIO-Net has the smallest error, indicating that the chosen reduced-basis is reliable in representing density anomalies. The Argo-derived gridded observations behave similarly in the testing and training sets, as they incorporate all observations. In the testing set the error of PIO-Net has increased, PIO-Net exhibits greater accuracy at shallow layers but lower accuracy at depths of 100–200 m compared to other methods. However, PIO-Net demonstrates comparable accuracy to Argo-derived gridded data and has a higher resolution, which indicates its reliability.

4.2.2. *Methods comparison*

In this section, we evaluate the performance of the proposed PIO-Net against two benchmark methods trained on Argo observational data: a Long Short-Term Memory network (LSTM) (Hochreiter and Schmidhuber, 1997) and a Feedforward Neural Network (FFNN). Both the LSTM and FFNN take sea surface density anomalies and the corresponding latitude—longitude coordinates as inputs, and predict subsurface density anomalies at the same locations. The LSTM architecture

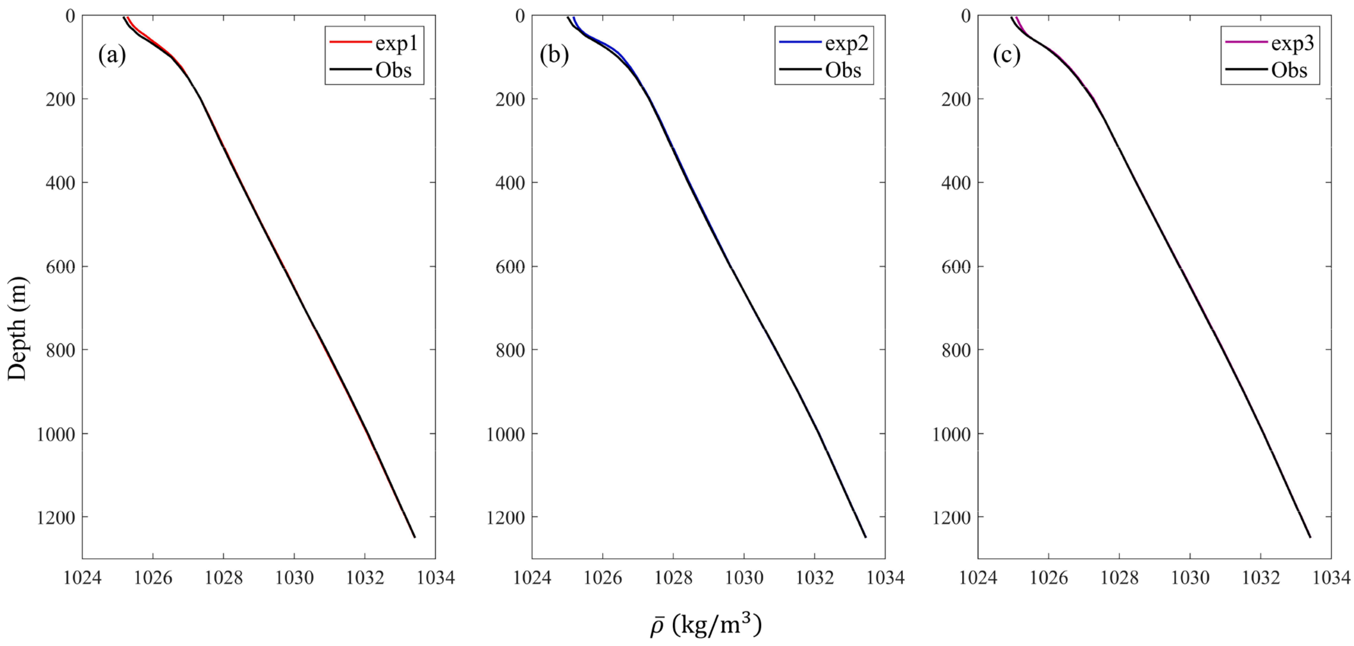

Fig. 9. The vertical distribution of the mean densities derived from Argo (black solid line) and PIO-Net for exp1 (a), exp2 (b) and exp3 (c).

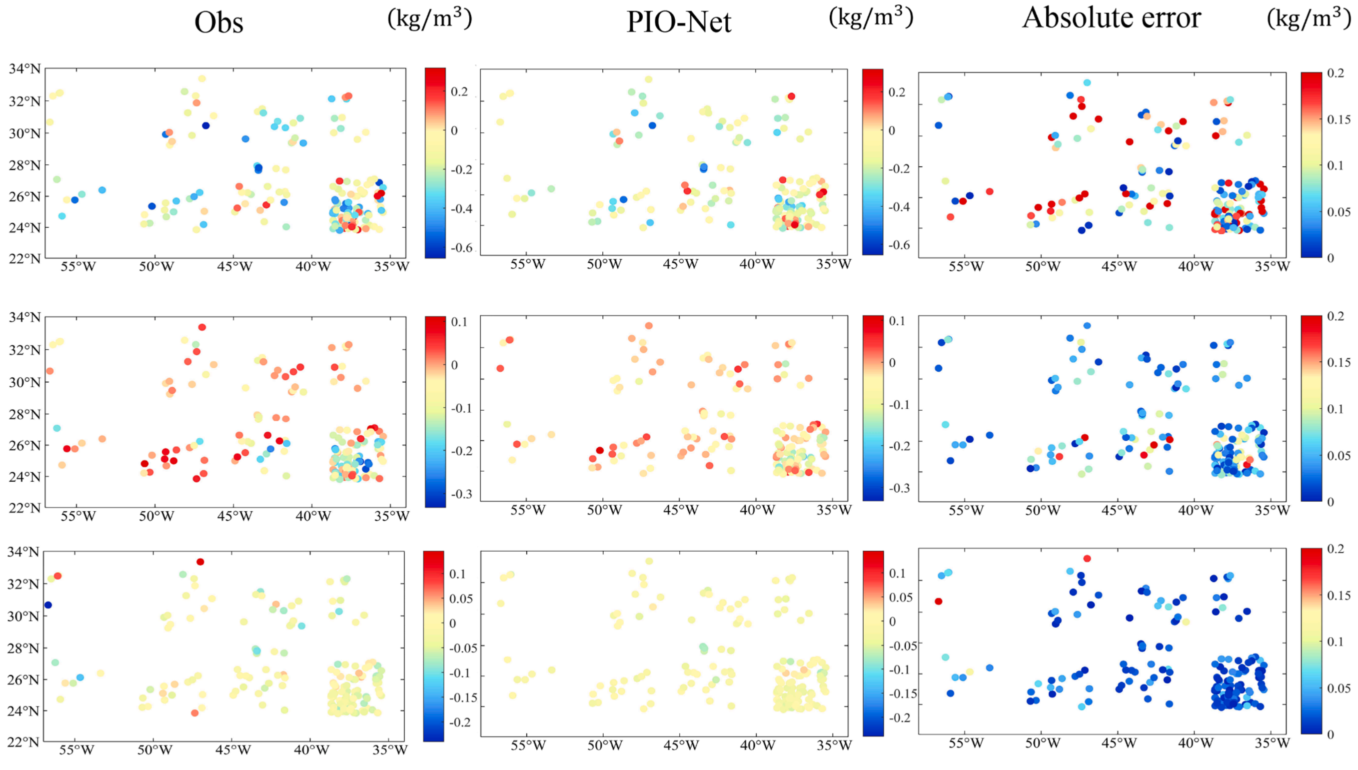

Fig. 10. Horizontal distribution of Argo-derived (left) and PIO-Net (middle) density anomalies and absolute differences between them at three test depths.

follows Chen et al. (2023), while the FFNN consists of two hidden layers with 100 neurons each.

In contrast to the point-wise predictions generated by the LSTM and FFNN, PIO-Net produces full horizontal subsurface density anomaly fields. To make a comparison of predictive accuracy, the outputs of PIO-Net are spatially interpolated to the Argo observation locations to compute the RMSE, whereas the RMSE values for the LSTM and FFNN are derived from the point-wise predictions.

Table 4 reports the RMSE values of PIO-Net (with 50 and 250 neurons, using 55 basis functions), LSTM, and FFNN. The underlined values indicate the highest precision achieved in each experiment. The PIO-Net with 250 neurons shows consistently higher accuracy than its 50-neuron counterpart in all experiments except exp1, where both configurations exhibit comparable performance. This may be attributed to the limited training data in exp1, where the benefits of increased model capacity are constrained by insufficient data diversity. Overall, PIO-Net achieves superior accuracy across all experiments, validating the reliability in subsurface density reconstruction. Additionally, PIO-Net's capability to directly output high-resolution density fields provides a practical advantage. Furthermore, in exp1 where training data are severely limited,

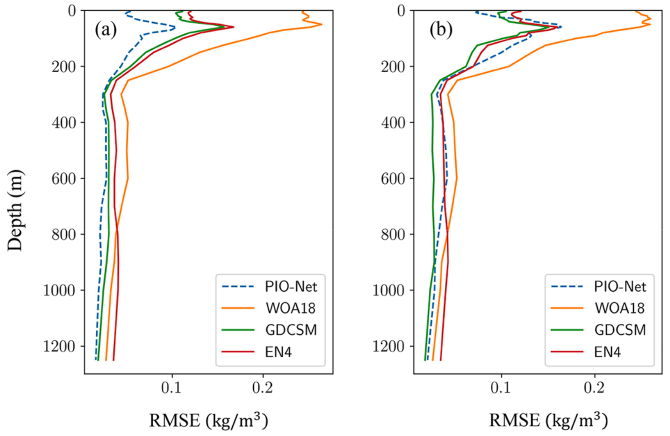

Fig. 11. Vertical RMSE distribution between observations and PIO-Net (blue dotted line), WOA18 climatology (orange line), GDCSM_Argo product (green line) and EN4 (red line) in training set (a) and testing set (b).

Table 4
The mean RMSEs of different methods.

Method	PIO-Net (50)	PIO-Net (250)	LSTM	FFNN
exp1	0.0846	0.0869	0.1086	0.1003
exp2	0.1003	0.0850	0.1081	0.1055
exp3	0.0884	0.0773	0.0902	0.0915

PIO-Net exhibits particularly enhanced performance, highlighting the benefits of incorporating physical constraints and the pretraining strategy in data-sparse scenarios.

To integrate physical knowledge into the learning process, the proposed PIO-Net incorporates a reduced-order form of the QG equation into the loss function. As a foundational model in large-scale ocean dynamics, the QG equation approximates key fluid motion laws, provides an effective framework for representing stratified flow structures and the impact of density variations.

By minimizing both the residuals of the reduced-order equation and the discrepancies between network predictions and observational targets, the training process simultaneously leverages sparse data and enforces physical constraints. These constraints act as physics-based priors, embedding the governing equations' structural form and the underlying dynamical terms into the model. As a result, the network's inputs and outputs are guided to approximately satisfy the physical laws.

Moreover, the incorporation of data-driven constraints allows the model to infer unknown terms in the reduced-order equation. This not only enhances the model's adaptability to real-world ocean variability but also reduce the errors introduced by simplifications. Overall, this physics-informed learning framework improves the interpretability and prediction accuracy, particularly in data-limited regimes where traditional models or purely data-driven methods may underperform.

4.2.3. Possible origins of reconstruction fields' errors

The estimation of density profiles is subject to several error sources. First, uncertainty in the observed data is one of the causes of the model's error, the L4 sea surface data used in this study still have various types of errors from the instrument observation errors, interpolation algorithm errors, and errors caused by weather. These inaccuracies lead to regional biases and discrepancies between the satellite-derived sea surface data and observations taken in the same location. Since the PIO-Net model is highly dependent on input data, systematic errors or noise in the training dataset can propagate into the learned patterns. For instance, if the satellite SSD data used for training exhibit a systematic underestimation, the network will assimilate these biases, potentially resulting in a generalized underestimation of salinity profiles. Fig. 12 displays the density anomalies difference curve between ESA-WOC and Argo at 4 m, as well as between PIO-Net and Argo at 4 m and 400 m with the number of test points. It can be seen that they exhibit similar variation curves, which once again indicates that the difference between satellite-derived sea surface data and Argo is a factor affecting the estimation accuracy of the model. The difference between the satellite and Argo observations affects not only the surface reconstruction, but also the internal estimation. Although PIO-Net integrates physical constraints, observational errors may introduce anomalous samples, misleading the learning of dynamic relationships and impairing the model's generalization capability.

Additionally, the improved PIO-Net incorporates a pre-training stage that utilizes extensive reanalysis data to establish a knowledge-guided initialization, which enables the network to capture fundamental spatial patterns and dynamic features inherent in the training data, facilitating more efficient convergence and enhanced performance during the fine-tuning with in situ observations. However, substantial disparities between the pre-training and fine-tuning datasets may introduce biases, potentially compromising reconstruction accuracy. This effect is particularly pronounced in data-sparse regions or areas exhibiting strong spatial variability, where the model relies on limited observations to determine fitting coefficients and reconstruct the complete density anomaly field. Undoubtedly, increasing observational coverage would significantly improve the reconstruction quality.

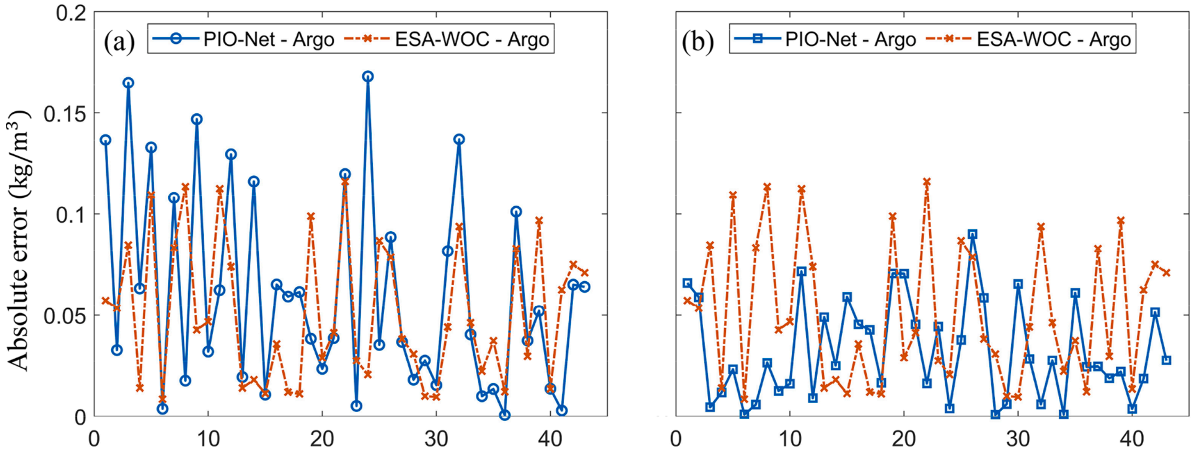

Fig. 12. Absolute differences in density anomalies between ESA-WOC and Argo at 4 m, as well as between PIO-Net and Argo at (a) 4 m and (b) 400 m, with respect to the number of test points.

Moreover, reconstruction errors may also stem from the use of reduced basis functions derived from HYCOM simulations, which might not fully represent the true variability observed in observational datasets.

5. Conclusions and discussions

In this paper, the accuracy and reliability of the PIO-Net model to estimate SDAs from sea surface information together with the effect of varying the number of reduced-basis on three-dimensional density reconstruction are first evaluated using HYCOM data, primarily through quantitative evaluation using RMSE. The results demonstrate that, the PIO-Net model can accurately reconstruct ocean internal density profile, and within a specific range of numbers, enriching the reduced-basis enhances the accuracy of the density estimation. In the case of the optimal reduced-basis configuration, the maximum time-averaged RMSE remains below 0.08. Compared to the reanalysis data, the density field reconstructed by the PIO-Net effectively preserves the signals of meso- and micro-scale phenomena, which is helpful for the further study of meso-and micro-scale processes. A new strategy is then developed in this work that uses unevenly distributed measurement data and satellite-derived observations to train the PIO-Net to project a more credible three-dimensional density field from the satellite data, which based on the physical relationships learned in the reanalysis data, combined with information from observations, to provide a more precise surface-subsurface relationship. Independent Argo observations are used to evaluate the PIO-Net reconstructed density field, demonstrating that the reconstructed fields accurately capture vertical density changes with precision and are well-aligned with the spatial distribution of Argo data. Experiments to study the effect of pre-training on reconstruction show that that leveraging the knowledge gained through pre-training can improve the accuracy of underwater density estimation, especially when the observations is limited and the training data for the pre-training and re-training phases contain similar relationships. This improvement has the potential to address the current uneven distribution of Argo floats, providing more reliable estimates in data-poor regions. The accuracy of the proposed method is further validated through comparisons between the PIO-Net-reconstructed density fields and gridded Argo products. In addition, relative to purely data-driven neural networks, the proposed method achieves both higher reconstruction accuracy and greater inference efficiency.

However, the proposed method also has limitations, firstly, there is no definitive method for selecting a set of reduced-basis that perfectly aligns with observational data, yet the selection of reduced-basis being a critical factor as inappropriate choices can introduce errors into the reconstruction process. Secondly, choosing regions with similar dynamical processes to train a PIO-Net model is beneficial for estimation. Since PIO-Net is built upon simplified dynamics, it heavily relies on training data to infer the unknown terms in the governing equations. This helps compensate for the limitations of the simplified physical models and allows the PIO-Net to adapt to the available data. As a result, the accuracy of the predictions is inherently constrained by the dynamical patterns captured in the training set. However, the relationship between surface signals and subsurface density can vary significantly across different regions. When applied to regions with substantially different dynamical characteristics, PIO-Net's performance may be various because the different physical knowledge contained in the data will ultimately affect the physical model constructed. Therefore, different PIO-Net models need to be trained for prediction. Thirdly, although we compensate for the limited number of observations by utilizing the knowledge gained from the reanalysis data, the inherent differences between the two require a certain amount of observations to correct the model, especially in regions where the two are significantly different. Therefore, applying the proposed methodology to regions with very limited observations remains a challenge. In addition, the error between satellite-derived observation and Argo measurement also affect the estimation accuracy, further investigation is necessary to clarify the connection between satellite SSD and Argo SSD.

In summary, PIO-Net is a reliable approach to project sea surface data into the deep ocean, producing high-resolution ocean data that can aid in studying intricate density changes. Besides, PIO-Net provides the ability to reconstruct underwater density fields when direct deep-sea observations are insufficient, improving our ability to detect ocean structural and dynamic changes, especially in the context of global warming. We will focus not only on enhancing the accuracy of the reduced-basis representations but also on investigating the role of various input parameters in improving reconstruction performance in the future work. Previous studies have demonstrated that incorporating additional sea surface variables, such as sea surface height and velocity, can significantly contribute to reconstructing three-dimensional ocean structures, as these variables are physically linked to subsurface dynamics. Thus, one can extend PIO-Net to a multi-input operator network architecture that integrates these parameters to provide a more comprehensive representation of surface conditions. In addition, more explicit positional information can be included in the inputs to improve the generalization ability of the model across different oceanic regions.

CRediT authorship contribution statement

Yuanhong Chen: Writing – review & editing, Writing – original draft, Validation, Methodology, Conceptualization; **Chunxin Yuan:** Writing – review & editing, Formal analysis; **Xiang Sun:** Writing – review & editing, Investigation; **Zhen Gao:** Writing – review & editing, Supervision, Project administration, Funding acquisition.

Data availability

Data will be made available on request.

Declaration of competing interest

The authors declare that they have no known competing financial interests or personal relationships that could have appeared to influence the work reported in this paper.

Acknowledgments

The authors would like to thank the reviewers for their valuable suggestions on the manuscript. This study is partially supported by the National Natural Science Foundation of China (12371435,12201592), Taishan Scholars Program (tsqn202211059), Shandong Provincial Natural Science Foundation (ZR2023MA043), and the Fundamental Research Funds for the Central Universities (202265005, 202264006, 202264007).

Appendix A. Brief Introduction of PIO-Net

QG theory shows that the geostrophic stream function is derived from the potential vorticity and the top/bottom densities under the assumption of QG-balanced motions as follows:

$$\begin{cases} \mathcal{L}\Psi + \frac{\partial}{\partial z}\left(\frac{f_0^2}{N^2}\frac{\partial \Psi}{\partial z}\right) = q, \quad -H < z < 0, \quad (x,y) \in \Omega, \\ \left.\frac{\partial \Psi}{\partial z}\right|_{z=0} = \frac{b_s}{f_0}, \quad (x,y) \in \Omega, \\ \left.\frac{\partial \Psi}{\partial z}\right|_{z=-H} = 0, \quad (x,y) \in \Omega, \end{cases} \tag{A.1}$$

where $\mathcal{L} = \left(\frac{\partial^2}{\partial x^2} + \frac{\partial^2}{\partial y^2}\right)$, $\Psi = p\left(\rho_0 f_0\right)^{-1}$ is the stream function with p implying the pressure, N^2 is the $\mathrm{Brunt-Väsälä}$ frequency, q represents the potential vorticity anomaly, and $b_s = -g\rho_s^a\rho_0^{-1}$ denotes the surface buoyancy anomaly. The state of the corresponding density anomaly ρ^a is given by $\rho^a = -\frac{\rho_0 f_0}{g}\frac{\partial \Psi}{\partial z}$. After discretizing the Eq. (A.1) on a staggered

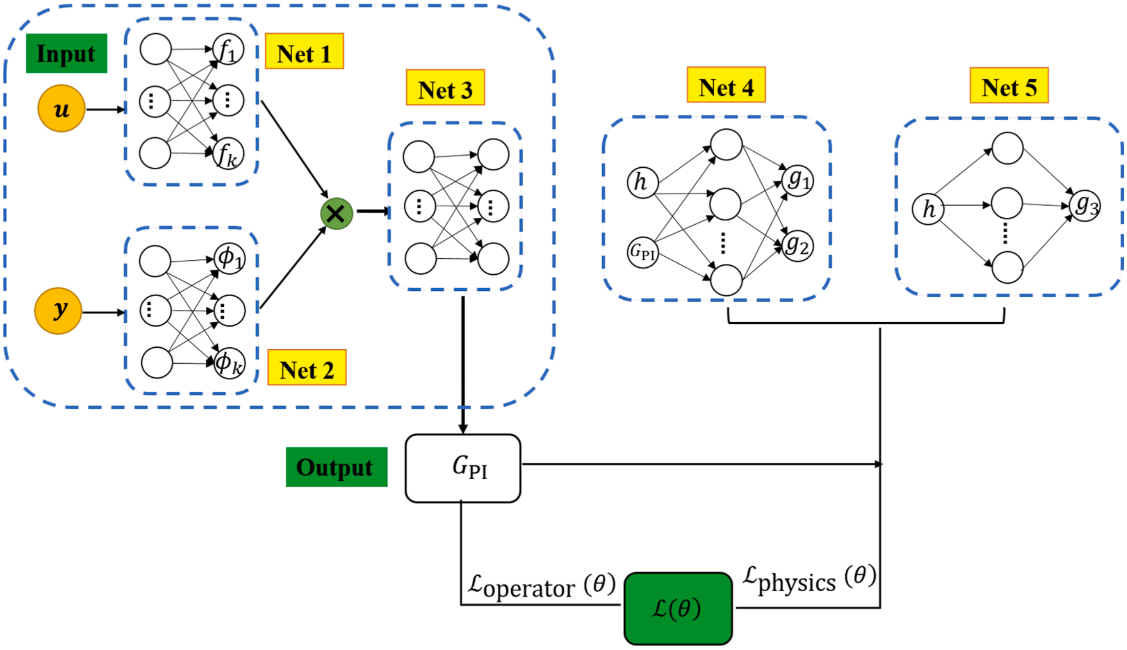

Fig. A.1. Structure of PIO-Net.

grid X and using a suitable partial differential equation solver, such as the finite difference method, the following ordinary differential equation can be obtained

$$\begin{cases} \mathcal{L}_h \boldsymbol{\Psi}_h + \frac{d}{dz}\left(\frac{f_0^2}{N^2}\frac{d\boldsymbol{\Psi}_h}{dz}\right) = \mathbf{q}, \quad -H < z < 0, \\ \left.\frac{d\boldsymbol{\Psi}_h}{dz}\right|_{z=0} = f_0^{-1}\mathbf{b}_s, \\ \left.\frac{d\boldsymbol{\Psi}_h}{dz}\right|_{z=-H} = 0, \end{cases}$$

where $\mathbf{q}$ and $\mathbf{b}_s$ are the discretized forms of the potential vorticity anomaly q, and the surface buoyancy anomaly b_s, respectively. $\mathcal{L}_h$ denotes the linear operator derived from $\mathcal{L}$. For ease of calculation and reduction of calculation costs, $\boldsymbol{\Psi}_h$ is approximated as a linear combination of a set of bases

$$\boldsymbol{\Psi}_h\left(z, \mathbf{b}_s\right) \approx \sum_{i=1}^{n} \alpha_i\left(z, \mathbf{b}_s\right)\psi_i = \mathbf{V}\boldsymbol{\alpha}\left(z, \mathbf{b}_s\right),$$

and suppose $\boldsymbol{\alpha}$ satisfies the governing equation of the following form

$$\begin{cases} c\mathbf{V}^{\mathrm{T}}\mathcal{L}_h(\mathbf{V}\boldsymbol{\gamma}) + g_1\left(h, \overline{\frac{d\boldsymbol{\gamma}}{dh}}\right)\frac{d\boldsymbol{\gamma}}{dh} + g_2\left(h, \overline{\frac{d\boldsymbol{\gamma}}{dh}}\right)\frac{d^2\boldsymbol{\gamma}}{d^2h} \\ = g_3(h)\mathbf{V}^{\mathrm{T}}\boldsymbol{\rho}_s^a, \\ \quad -H_f < h < 0, \\ \left.\frac{d\boldsymbol{\gamma}}{dh}\right|_{h=0} = -f^{-1}\mathbf{V}^{\mathrm{T}}\boldsymbol{\rho}_s^a, \ \left.\frac{d\boldsymbol{\gamma}}{dh}\right|_{h=-H_f} = 0, \\ \mathbf{V}^{\mathrm{T}}\boldsymbol{\rho}^a = -f\frac{d\boldsymbol{\gamma}}{dz}, \end{cases} \tag{A.2}$$

where $c = 500^2 \times 10^5$, $n_z = N^2 \times 10^5$, $\tilde{\mathbf{q}} = c\mathbf{q}^{-1}$ and $H_f = H/500$, the bar of the vector denotes the mean of the vector, the unknown functions g_1, g_2 depend on the variable h and the mean of the derivative of vector $\boldsymbol{\gamma}$ with respect to h, and unknown function g_3 depend on variable h.

Eq. (A.2) is regarded as a differential equation parameterized by $f^{-1}\mathbf{V}^{\mathrm{T}}\boldsymbol{\rho}_s^a$ that to compute SSDA in the presence of given values for g_1, g_2, and g_3. To to predict the variable $\boldsymbol{\gamma}$ and estimate g_1, g_2, and g_3, PIO-Net method is proposed with the architecture is shown in Fig. A.1. The input of PIO-Net is $\boldsymbol{u} = f^{-1}\boldsymbol{\nu}_{z_0}$ and $\boldsymbol{y} = h$ and the output is to estimate $\boldsymbol{\gamma}$, Net 4 and Net 5 are two feedforward neural networks, which are used to predict the unknown functions g_1, g_2 and g_3. The loss function of the PIO-Net is defined as

$$\mathcal{L}(\theta) = c_1\mathcal{L}_{\text{operator}}(\theta) + c_2\mathcal{L}_{\text{physics}}(\theta),$$

where $\mathcal{L}_{\text{operator}}(\theta)$ is the mean squared error between the network output and the projection coefficient of the density anomaly profile at N_t different times, given by

$$\mathcal{L}_{\text{operator}}(\theta) = \frac{1}{N_s m}\sum_{i=1}^{N_s}\sum_{j=1}^{m}\left|-f\frac{dG_{\mathrm{PI}}\left(f^{-1}\boldsymbol{\nu}_{z_0}^i\right)\left(h_j\right)}{dh} - \boldsymbol{\nu}_{z_j}^i\right|^2.$$

$\mathcal{L}_{\text{physics}}(\theta)$ represents the mean squared residual error on the reduced-order equation Eq. (A.2), evaluated over a designated set of residual points to integration of physical laws into the neural network

$$\begin{aligned} \mathcal{L}_{\text{physics}}(\theta) = {} & \frac{1}{N_s N_t}\sum_{i=1}^{N_s}\sum_{j=1}^{N_t}\left|g_{nn}\left(f^{-1}\boldsymbol{\nu}_{z_0}^i\right)\left(h_j^{(i)}\right)\right|^2 \\ & + \frac{1}{N_s}\sum_{i=1}^{N_s}\left|\frac{dG_{\mathrm{PI}}\left(f^{-1}\boldsymbol{\nu}_{z_0}^i\right)\left(h_0\right)}{dh} + f^{-1}\mathbf{V}^{\mathrm{T}}\boldsymbol{\rho}_{z_0}^i\right|^2 \\ & + \frac{1}{N_s}\sum_{i=1}^{N_s}\left|\frac{dG_{\mathrm{PI}}\left(f^{-1}\boldsymbol{\nu}_{z_0}^i\right)\left(-H_f\right)}{dh}\right|^2, \end{aligned}$$

with

$$\begin{aligned} g_{nn}\left(f^{-1}\boldsymbol{\nu}_{z_0}^i\right)\left(h_j^{(i)}\right) = {} & c\mathbf{V}^{\mathrm{T}}\mathcal{L}_h\left(\mathbf{V}G_{\mathrm{PI}}\left(f^{-1}\boldsymbol{\nu}_{z_0}^i\right)\left(h_j^{(i)}\right)\right) \\ & + g_1\left(h, g_j^i\right)\frac{dG_{\mathrm{PI}}\left(f^{-1}\boldsymbol{\nu}_{z_0}^i\right)\left(h_j^{(i)}\right)}{dh} \\ & + g_2\left(h, g_j^i\right)\frac{d^2G_{\mathrm{PI}}\left(f^{-1}\boldsymbol{\nu}_{z_0}^i\right)\left(h_j^{(i)}\right)}{dh^2} \\ & - g_3(h)\mathbf{V}^{\mathrm{T}}\boldsymbol{\rho}_{\boldsymbol{s}}, \end{aligned}$$

where $\{h_j^{(i)}\}_{i=1}^{N_t}$ are N_t collocations points uniformly selected in $[-H_f, 0]$, and

$$g_j^i = \overline{\frac{dG_{\mathrm{PI}}\left(f^{-1}\boldsymbol{\nu}_{z_0}^i\right)\left(h_j^{(i)}\right)}{dh}}.$$

A detailed introduction can be found in Chen et al. (2024).

References

Ali, M.M., Swain, D., Weller, R.A., 2004. Estimation of ocean subsurface thermal structure from surface parameters: a neural network approach. Geophys. Res. Lett. 31 (20). https://doi.org/10.1029/2004GL021192

Assassi, C., Morel, Y., Vandermeirsch, F., Chaigneau, A., Pegliasco, C., Morrow, R., Colas, F., Fleury, S., Carton, X., Klein, P., Cambra, R., 2016. An index to distinguish surface- and subsurface-intensified vortices from surface observations. J. Phys. Oceanogr. 46 (8), 2529–2552. https://doi.org/10.1175/JPO-D-15-0122.1

Bao, S., Zhang, R., Wang, H., Yan, H., Yu, Y., Chen, J., 2019. Salinity profile estimation in the pacific ocean from satellite surface salinity observations. J. Atmos. Oceanic Technol. 36 (1), 53–68. https://doi.org/10.1175/JTECH-D-17-0226.1

Blumberg, A.F., Mellor, G.L., 1987. A Description of a Three-Dimensional Coastal Ocean Circulation Model. American Geophysical Union (AGU). pp. 1–16. https://doi.org/10.1029/CO004p0001

Buongiorno Nardelli, B., 2020a. ESA-WOC North Atlantic Sea Surface Salinity maps from a multivariate combination of satellite and in situ surface measurements (2010–2018). Zenodo v1.0. https://doi.org/10.5281/zenodo.3943813

Buongiorno Nardelli, B., 2020b. A deep learning network to retrieve ocean hydrographic profiles from combined satellite and in situ measurements. Remote Sens. 12 (19). https://doi.org/10.3390/rs12193151

Buongiorno Nardelli, B., Guinehut, S., Pascual, A., Drillet, Y., Ruiz, S., Mulet, S., 2012. Towards high resolution mapping of 3-d mesoscale dynamics from observations. Ocean Sci. 8 (5), 885–901. https://doi.org/10.5194/os-8-885-2012

Buongiorno Nardelli, B., Santoleri, R., 2005. Methods for the reconstruction of vertical profiles from surface data: multivariate analyses, residual GEM, and variable temporal signals in the north pacific ocean. J. Atmos. Oceanic Technol. 22 (11), 1762–1781. https://doi.org/10.1175/JTECH1792.1

Carnes, M.R., Teague, W.J., Mitchell, J.L., 1994. Inference of subsurface thermohaline structure from fields measurable by satellite. J. Atmos. Oceanic Technol. 11 (2), 551–566. https://doi.org/10.1175/1520-0426(1994)011 < 0551:IOSTSF > 2.0.CO;2

Chassignet, E.P., Hurlburt, H.E., Smedstad, O.M., Halliwell, G.R., Hogan, P.J., Wallcraft, A.J., Baraille, R., Bleck, R., 2007. The HYCOM (HYbrid coordinate ocean model) data assimilative system. J. Mar. Syst. 65 (1), 60–83. Marine Environmental Monitoring and Prediction. https://doi.org/10.1016/j.jmarsys.2005.09.016

Chen, C., Yang, K., Ma, Y., Wang, Y., 2018. Reconstructing the subsurface temperature field by using sea surface data through self-organizing map method. IEEE Geosci. Remote Sens. Lett. 15 (12), 1812–1816. https://doi.org/10.1109/LGRS.2018.2866237

Chen, Y., Liu, L., Chen, X., Wei, Z., Sun, X., Yuan, C., Gao, Z., 2023. Data driven three-dimensional temperature and salinity anomaly reconstruction of the northwest pacific ocean. Front. Mar. Sci. 10, 1121334.

Chen, Y., Liu, L., Yuan, C., Sun, X., Chen, X., Wei, Z., Gao, Z., 2024. Physics-informed deep operator learning based on reduced-order modeling for retrieving the ocean interior density from the surface. J. Geophys. Res. Oceans 129 (2), e2023JC019941. https://doi.org/10.1029/2023JC019941

Chen, Z., Wang, X., Liu, L., 2020. Reconstruction of three-dimensional ocean structure from sea surface data: an application of isQG method in the southwest indian ocean. J. Geophys. Res. Oceans 125 (6), e2020JC016351. https://doi.org/10.1029/2020JC016351

Contractor, S., Roughan, M., 2021. Efficacy of feedforward and LSTM neural networks at predicting and gap filling coastal ocean timeseries: oxygen, nutrients, and temperature. Front. Mar. Sci. 8. https://doi.org/10.3389/fmars.2021.637759

Cummings, J.A., 2005. Operational multivariate ocean data assimilation. Q. J. R. Meteorolog. Soc. 131 (613), 3583–3604. https://doi.org/10.1256/qj.05.105

Cummings, J.A., Smedstad, O.M., 2013. Variational Data Assimilation for the Global Ocean. Springer Berlin Heidelberg, Berlin, Heidelberg. pp. 303–343. https://doi.org/10.1007/978-3-642-35088-7_13

Dean, R., Belbéoch, M., Howard, F., Garzoli, S., Gould, W., Grant, F., Mark, I., Brian, K., Klein, B., Traon, P.-Y., Mork, K., Owens, W., Pouliquen, S., Ravichandran, M., Riser, S., Sterl, A., Toshio, S., Suk, M.-s., Sutton, P., Jianping, X., 2009. Argo: the challenge of continuing 10 years of progress. Oceanography 22. https://doi.org/10.5670/oceanog.2009.65

Dong, C., Xu, G., Han, G., Bethel, B.J., Xie, W., Zhou, S., 2022. Recent developments in artificial intelligence in oceanography. Ocean-Land-Atmosphere Res. 2022. https://doi.org/10.34133/2022/9870950

Doshi-Velez, F., Kim, B., 2017. Towards a rigorous science of interpretable machine learning. arXiv preprint arXiv:1702.08608.

Fiedler, P.C., 1988. Surface manifestations of subsurface thermal structure in the california current. J. Geophys. Res. Oceans 93 (C5), 4975–4983. https://doi.org/10.1029/JC093iC05p04975

Fischer, M., Latif, M., Flügel, M., Ji, M., 1997. The impact of data assimilation on ENSO simulations and predictions. Mon. Weather Rev. 125 (5), 819–830. https://doi.org/10.1175/1520-0493(1997)125 < 0819:TIODAO > 2.0.CO;2

Fofonoff, N., Millard, R., 1983. Algorithms for computation of fundamental properties of seawater. UNESCO Tech. Pap. Mar. Sci. 44, 25–77.

Fox-Kemper, B., Adcroft, A., Böning, C.W., Chassignet, E.P., Curchitser, E., Danabasoglu, G., Eden, C., England, M.H., Gerdes, R., Greatbatch, R.J., Griffies, S.M., Hallberg, R.W., Hanert, E., Heimbach, P., Hewitt, H.T., Hill, C.N., Komuro, Y., Legg, S., Le Sommer, J., Masina, S., Marsland, S.J., Penny, S.G., Qiao, F., Ringler, T.D., Treguier, A.M., Tsujino, H., Uotila, P., Yeager, S.G., 2019. Challenges and prospects in ocean circulation models. Front. Mar. Sci. 6. https://doi.org/10.3389/fmars.2019.00065

Gallaudet, T.C., Simpson, J.J., 1994. An empirical orthogonal function analysis of remotely sensed sea surface temperature variability and its relation to interior oceanic processes off baja california. Remote Sens. Environ. 47 (3), 375–389. https://doi.org/10.1016/0034-4257(94)90105-8

Good, S.A., Martin, M.J., Rayner, N.A., 2013. En4: quality controlled ocean temperature and salinity profiles and monthly objective analyses with uncertainty estimates. J. Geophys. Res. Oceans 118 (12), 6704–6716. https://doi.org/10.1002/2013JC009067

Guinehut, S., Dhomps, A.-L., Larnicol, G., Le Traon, P.Y., 2012. High resolution 3-d temperature and salinity fields derived from in situ and satellite observations. Ocean Sci. 8 (5), 845–857. https://doi.org/10.5194/os-8-845-2012

Guo, Y., Liu, Y., Oerlemans, A., Lao, S., Wu, S., Lew, M.S., 2016. Deep learning for visual understanding: a review. Neurocomputing 187, 27–48. Recent Developments on Deep Big Vision. https://doi.org/10.1016/j.neucom.2015.09.116

Held, I.M., Pierrehumbert, R.T., Garner, S.T., Swanson, K.L., 1995. Surface quasi-geostrophic dynamics. J. Fluid Mech. 282, 1–20. https://doi.org/10.1017/S0022112095000012

Hochreiter, S., Schmidhuber, J., 1997. Long short-term memory. Neural Comput. 9 (8), 1735–1780.

Isern-Fontanet, J., Chapron, B., Lapeyre, G., Klein, P., 2006. Potential use of microwave sea surface temperatures for the estimation of ocean currents. Geophys. Res. Lett. 33 (24). https://doi.org/10.1029/2006GL027801

Isern-Fontanet, J., Lapeyre, G., Klein, P., Chapron, B., Hecht, M.W., 2008. Three-dimensional reconstruction of oceanic mesoscale currents from surface information. J. Geophys. Res. Oceans 113 (C9). https://doi.org/10.1029/2007JC004692

Jean-Michel, L., Eric, G., Romain, B.-B., Gilles, G., Angélique, M., Marie, D., Clément, B., Mathieu, H., Olivier, L.G., Charly, R., Tony, C., Charles-Emmanuel, T., Florent, G., Giovanni, R., Mounir, B., Yann, D., Pierre-Yves, L.T., 2021. The copernicus global 1/12° oceanic and sea ice GLORYS12 reanalysis. Front. Earth Sci. 9. https://doi.org/10.3389/feart.2021.698876

Johnson, G.C., Hosoda, S., Jayne, S.R., Oke, P.R., Riser, S.C., Roemmich, D., Suga, T., Thierry, V., Wijffels, S.E., Xu, J., 2022. Argo—two decades: global oceanography, revolutionized. Ann. Rev. Mar. Sci. 14 (1), 379–403. https://doi.org/10.1146/annurev-marine-022521-102008

Khedouri, E., Szczechowski, C., Cheney, R., 1983. Potential oceanographic applications of satellite altimetry for inferring subsurface thermal structure. In: Proceedings OCEANS '83, pp. 274–280. https://doi.org/10.1109/OCEANS.1983.1152138

Klein, P., Isern-Fontanet, J., Lapeyre, G., Roullet, G., Danioux, E., Chapron, B., Le Gentil, S., Sasaki, H., 2009. Diagnosis of vertical velocities in the upper ocean from high resolution sea surface height. Geophys. Res. Lett. 36 (12). https://doi.org/10.1029/2009GL038359

Klein, P., Lapeyre, G., Siegelman, L., Qiu, B., Fu, L.-L., Torres, H., Su, Z., Menemenlis, D., Le Gentil, S., 2019. Ocean-scale interactions from space. Earth Space Sci. 6 (5), 795–817. https://doi.org/10.1029/2018EA000492

Klemas, V., Yan, X.-H., 2014. Subsurface and deeper ocean remote sensing from satellites: an overview and new results. Prog. Oceanogr. 122, 1–9. https://doi.org/10.1016/j.pocean.2013.11.010

Lapeyre, G., Klein, P., 2006. Dynamics of the upper oceanic layers in terms of surface quasigeostrophy theory. J. Phys. Oceanogr. 36 (2), 165–176. https://doi.org/10.1175/JPO2840.1

Liu, L., Peng, S., Huang, R.X., 2017. Reconstruction of ocean's interior from observed sea surface information. J. Geophys. Res. Oceans 122 (2), 1042–1056. https://doi.org/10.1002/2016JC011927

Liu, L., Peng, S., Wang, J., Huang, R.X., 2014. Retrieving density and velocity fields of the ocean's interior from surface data. J. Geophys. Res. Oceans 119 (12), 8512–8529. https://doi.org/10.1002/2014JC010221

Liu, L., Xue, H., Sasaki, H., 2019. Reconstructing the ocean interior from high-resolution sea surface information. J. Phys. Oceanogr. 49 (12), 3245–3262. https://doi.org/10.1175/JPO-D-19-0118.1

Liu, Z.H., Li, Z.Q., Lu, S.L., Wu, X.F., Sun, C.H., Xu, J.P., 2021. Scattered dataset of global ocean temperature and salinity profiles from the international argo program. J. Glob. Change Data Discov. 5 (3), 312–321. https://doi.org/10.3974/geodp.2021.03.09

Lu, W., Su, H., Yang, X., Yan, X.-H., 2019. Subsurface temperature estimation from remote sensing data using a clustering-neural network method. Remote Sens. Environ. 229, 213–222. https://doi.org/10.1016/j.rse.2019.04.009

Maes, C., Behringer, D., Reynolds, R.W., Ji, M., 2000. Retrospective analysis of the salinity variability in the western tropical pacific ocean using an indirect minimization approach. J. Atmos. Oceanic Technol. 17 (4), 512–524. https://doi.org/10.1175/1520-0426(2000)017 < 0512:RAOTSV > 2.0.CO;2

Mellor, G., Hakkinen, S., Ezer, T., Patchen, R., 2002. Ocean forecasting: conceptual basis and applications. Springer Science & Business Media, pp. 55–72.

Meng, L., Yan, C., Zhuang, W., Zhang, W., Geng, X., Yan, X.-H., 2022. Reconstructing high-resolution ocean subsurface and interior temperature and salinity anomalies from satellite observations. IEEE Trans. Geosci. Remote Sens. 60, 1–14. https://doi.org/10.1109/TGRS.2021.3109979

Meng, L., Yan, C., Zhuang, W., Zhang, W., Yan, X.-H., 2021. Reconstruction of three-dimensional temperature and salinity fields from satellite observations. J. Geophys. Res. Oceans 126 (11), e2021JC017605. https://doi.org/10.1029/2021JC017605

Meng, L., Yan, X.-H., 2022. Remote sensing for subsurface and deeper oceans: an overview and a future outlook. IEEE Geosci. Remote Sens. Mag. 10 (3), 72–92. https://doi.org/10.1109/MGRS.2022.3184951

Qiu, B., Chen, S., Klein, P., Ubelmann, C., Fu, L.-L., Sasaki, H., 2016. Reconstructability of three-dimensional upper-ocean circulation from SWOT sea surface height measurements. J. Phys. Oceanogr. 46 (3), 947–963. https://doi.org/10.1175/JPO-D-15-0188.1

Roarty, H., Cook, T., Hazard, L., George, D., Harlan, J., Cosoli, S., Wyatt, L., Alvarez Fanjul, E., Terrill, E., Otero, M., Largier, J., Glenn, S., Ebuchi, N., Whitehouse, B., Bartlett, K., Mader, J., Rubio, A., Corgnati, L., Mantovani, C., Griffa, A., Reyes, E., Lorente, P., Flores-Vidal, X., Saavedra-Matta, K.J., Rogowski, P., Prukpitikul, S., Lee, S.-H., Lai, J.-W., Guerin, C.-A., Sanchez, J., Hansen, B., Grilli, S., 2019. The global high frequency radar network. Front. Mar. Sci. 6. https://doi.org/10.3389/fmars.2019.00164

Roemmich, D., Johnson, G., Riser, S., Davis, R., Gilson, J., Owens, W., Garzoli, S., Schmid, C., Mark, I., 2009a. The argo program observing the global ocean with profiling floats. Oceanography 22. https://doi.org/10.5670/oceanog.2009.36

Roemmich, D., Johnson, G.C., Riser, S., Davis, R., Gilson, J., Owens, W.B., Garzoli, S.L., Schmid, C., Ignaszewski, M., 2009b. The argo program: observing the global ocean with profiling floats. Oceanography 22 (2), 34–43. https://doi.org/10.5670/oceanog.2009.36

Ronneberger, O., Fischer, P., Brox, T., 2015. U-Net: convolutional networks for biomedical image segmentation. In: Medical image computing and computer-assisted intervention–MICCAI 2015: 18th international conference, Munich, Germany, October 5–9, 2015, proceedings, part III 18. Springer, pp. 234–241.

Shi, X., Chen, Z., Wang, H., Yeung, D.-Y., Wong, W.-K., Woo, W.-c., 2015. Convolutional LSTM network: a machine learning approach for precipitation nowcasting. Adv. Neural Inf. Process. Syst. 28.

Stammer, D., 2005. Adjusting internal model errors through ocean state estimation. J. Phys. Oceanogr. 35 (6), 1143–1153. https://doi.org/10.1175/JPO2733.1

Su, H., Li, W., Yan, X.-H., 2018. Retrieving temperature anomaly in the global subsurface and deeper ocean from satellite observations. J. Geophys. Res. Oceans 123 (1), 399–410. https://doi.org/10.1002/2017JC013631

Su, H., Wang, A., Zhang, T., Qin, T., Du, X., Yan, X.-H., 2021. Super-resolution of subsurface temperature field from remote sensing observations based on machine learning. Int. J. Appl. Earth Obs. Geoinf. 102, 102440. https://doi.org/10.1016/j.jag.2021.102440

Su, H., Wu, X., Yan, X.-H., Kidwell, A., 2015. Estimation of subsurface temperature anomaly in the indian ocean during recent global surface warming hiatus from satellite measurements: a support vector machine approach. Remote Sens. Environ. 160, 63–71. https://doi.org/10.1016/j.rse.2015.01.001

Su, H., Zhang, H., Geng, X., Qin, T., Lu, W., Yan, X.-H., 2020. Open: a new estimation of global ocean heat content for upper 2000 m from remote sensing data. Remote Sens. 12 (14). https://doi.org/10.3390/rs12142294

Su, H., Zhang, T., Lin, M., Lu, W., Yan, X.-H., 2021b. Predicting subsurface thermohaline structure from remote sensing data based on long short-term memory neural networks. Remote Sens. Environ. 260, 112465. https://doi.org/10.1016/j.rse.2021.112465

Talley, L.D., Pickard, G.L., Emery, W.J., Swift, J.H., 2011. Chapter 6 - Data analysis concepts and observational methods. In: Talley, L.D., Pickard, G.L., Emery, W.J., Swift, J.H. (Eds.), Descriptive Physical Oceanography (Sixth Edition). Academic Press, Boston, Sixth edition. pp. 147–186. https://doi.org/10.1016/B978-0-7506-4552-2.10006-X

Tian, T., Cheng, L., Wang, G., Abraham, J., Wei, W., Ren, S., Zhu, J., Song, J., Leng, H., 2022. Reconstructing ocean subsurface salinity at high resolution using a machine learning approach. Earth Syst. Sci. Data 14 (11), 5037–5060. https://doi.org/10.5194/essd-14-5037-2022

Torres, R., Snoeij, P., Geudtner, D., Bibby, D., Davidson, M., Attema, E., Potin, P., Rommen, B., Floury, N., Brown, M., Traver, I.N., Deghaye, P., Duesmann, B., Rosich, B., Miranda, N., Bruno, C., L'Abbate, M., Croci, R., Pietropaolo, A., Huchler, M., Rostan, F., 2012. Gmes sentinel-1 mission. Remote Sens. Environ. 120, 9–24. The Sentinel Missions - New Opportunities for Science. https://doi.org/10.1016/j.rse.2011.05.028

Trenberth, K.E., 2015. Has there been a hiatus? Science 349 (6249), 691–692. https://doi.org/10.1126/science.aac9225

Trenberth, K.E., Fasullo, J.T., 2013. An apparent hiatus in global warming? Earth's Future 1 (1), 19–32. https://doi.org/10.1002/2013EF000165

Wang, J., Flierl, G.R., LaCasce, J.H., McClean, J.L., Mahadevan, A., 2013. Reconstructing the ocean's interior from surface data. J. Phys. Oceanogr. 43 (8), 1611–1626. https://doi.org/10.1175/JPO-D-12-0204.1

Wang, S., Teng, Y., Perdikaris, P., 2021. Understanding and mitigating gradient flow pathologies in physics-informed neural networks. SIAM J. Sci. Comput. 43 (5), A3055–A3081. https://doi.org/10.1137/20M1318043

Wu, X., Yan, X.-H., Jo, Y.-H., Liu, W.T., 2012. Estimation of subsurface temperature anomaly in the north atlantic using a self-organizing map neural network. J. Atmos. Oceanic Technol. 29 (11), 1675–1688. https://doi.org/10.1175/JTECH-D-12-00013.1

Xie, S.-P., Yu, K., 2017. What caused the global surface warming hiatus of 1998–2013? Curr. Clim. Change Rep. 3, 126–140. https://doi.org/10.1007/s40641-017-0063-0

Xu, D., Liu, Y., Kong, Y., 2025. A deep learning inversion method for 3d temperature structures in the south china sea with physical constraints. J. Mar. Sci. Eng. 13 (6). https://doi.org/10.3390/jmse13061061

Xue, S., Geng, X., Meng, L., Xie, T., Huang, L., Yan, X.-H., 2021. Hisea-1: the first c-band sar miniaturized satellite for ocean and coastal observation. Remote Sens. 13 (11). https://doi.org/10.3390/rs13112076

Yu, X., Yi, D.L., Wang, P., 2025. Enhancing ocean temperature and salinity reconstruction with deep learning: the role of surface waves. J. Mar. Sci. Eng. 13 (5). https://doi.org/10.3390/jmse13050910

Zhang, C., Wang, D., Liu, Z., Lu, S., Sun, C., Wei, Y., Zhang, M., 2022. Global gridded argo dataset based on gradient-dependent optimal interpolation. J. Mar. Sci. Eng. 10 (5). https://doi.org/10.3390/jmse10050650

Zhou, G., Han, G., Li, W., Wang, X., Wu, X., Cao, L., Li, C., 2023. High-resolution gridded temperature and salinity fields from argo floats based on a spatiotemporal four-dimensional multigrid analysis method. J. Geophys. Res. Oceans 128 (5), e2022JC019386. https://doi.org/10.1029/2022JC019386